

Atomic and electronic structures of an ultrathin Ni-deposited SiC(0001)-2×2 surface

Y. Hoshino,^{1,2,*} Y. Matsubara,¹ T. Nishimura,¹ and Y. Kido¹¹Department of Physics, Ritsumeikan University, Kusatsu, Shiga 525-8577, Japan²Department of Electronic Science and Engineering, Kyoto University, Katsura, Kyoto 615-8510, Japan

(Received 20 May 2005; revised manuscript received 6 October 2005; published 16 December 2005)

The atomic and electronic structures of the 6H-SiC(0001̄)-2×2 surface deposited with an ultrathin Ni(0.3–1.3 ML) layer before and after annealing were analyzed by high-resolution medium and low-energy ion scattering (MEIS/LEIS), photoelectron spectroscopy using synchrotron-radiation-light and reflection high-energy electron diffraction [1 ML=1.21×10¹⁵ atoms/cm²]. The Ni(0.3–1.3 ML)/SiC(0001̄) surfaces as-deposited and annealed at temperatures up to 600 °C show a pseudo-(1×3) diffraction pattern. Fourier transform from the reciprocal lattice points into the direct lattice reveals basically random arrangements of the (1×3), (1×2), and (1×1) supercells in each domain. It is also found that there are three types of domains taking slender rectangle shapes with long edges along the [121̄0], [1120], and [211̄0] directions, and Ni atoms on top of the surface are aligned along the direction making an 120° with respect to the above each edge to form one-dimensional (1×) chains. The valence band spectra show that the pseudo-(1×3) surface has a metallic character. Annealing at higher temperatures (>800 °C) leads to formation of a (2√3×2√3) surface. The MEIS analysis reveals the fact that Si (0.57±0.05 ML) and Ni (0.22±0.05 ML) adatoms are located on a Si adlayer (1 ML), which terminates the first C-Si bilayer. An azimuth-scan analysis using 2 keV He⁺ ions unveils the surface structure resembling that of the Ni/Si(111)-√19 rings proposed by [Parikh, Lee, and Bennett, *Surf. Sci.* **356**, 53 (1996)]. The surface electronic property is nonmetallic, probably due to a large interatomic distance of ~11 Å for Ni atoms in the neighboring (2√3×2√3) unit cell.

DOI: 10.1103/PhysRevB.72.235416

PACS number(s): 68.49.-h, 68.47.Fg, 73.20.At

I. INTRODUCTION

Silicon carbide has attracted much attention as the best candidate for high-temperature, high-power, and high-frequency electronic devices. Needless to say, metal/SiC contact is of great importance for device fabrication. So far, there have been a lot of studies on metal/SiC contacts from practical viewpoints.^{1–4} Unfortunately, the quantitative information is still insufficient concerning the initial growth processes of metal/SiC interfaces.^{5–7} In particular, there are only a few reports on the C-terminated (0001̄) surface, because of its large defect densities at oxide/SiC(0001̄) interfaces and of difficulties in controlling dopant concentrations. Recently, however, pyrogenic oxidation followed by annealing under hydrogen ambient has brought a breakthrough for considerable reduction of the interfacial defect densities.⁸ Therefore, now it is strongly required to characterize the oxidation and the metal/SiC contact formation for the C-terminated surface.

In the previous work, we analyzed the Ni-deposited SiC(0001)-√3×√3 surface.^{9–11} Si-adatoms (1/3 ML) exist on the top Si-C bilayer. The as-deposited Ni (1 ML) layer [1 ML for SiC(0001): 1.21×10¹⁵ atoms/cm²] is disordered and stacked almost uniformly without any reaction with the SiC substrate. Post-annealing at 400 °C leads to formation of an ordered NiSi₂ layer with thickness 1-2 Si-Ni-Si triple layers. A (4×4) superstructure appears by annealing at higher temperatures from 600 to 800 °C.

As is well known, the SiC(0001̄) surface takes several surface reconstructions dependent on sample preparation. We determined previously the surface structure of the Si-

enriched SiC(0001̄)-2×2 prepared by Si deposition of ~3.0 ML followed by annealing at 950 °C for 5 min.¹² Such a Si predeposition suppresses surface graphitization. The present study focuses on the atomic and electronic structures of an ultrathin Ni (0.3–1.3 ML) layer on the Si-rich SiC(0001̄)-2×2 surface as-deposited and post annealed. The surface structures are determined by high-resolution medium energy ion scattering (MEIS), low-energy ion scattering (LEIS), and high-energy electron diffraction (RHEED). The electronic properties obtained by photoelectron spectroscopy using synchrotron-radiation-light (SR-PES) are interpreted in terms of the surface atomic configurations. All the analyses were carried out *in situ* under ultrahigh vacuum (UHV) condition.

II. EXPERIMENT

We employed chemically and mechanically polished 6H-SiC(0001̄) wafers (N-doped) purchased from CREE Inc. and cut them into small pieces with a typical size of 10×10 mm². After cleaning the surface by a modified RCA method,¹³ the sample was introduced into an UHV chamber and degassed at 600 °C for 5 h. Then cooling it down to RT, a small amount of Si (~3 ML) was deposited by molecular beam epitaxy (MBE) and after that the sample was annealed at 950 °C for 5 min in UHV. Such a Si-cap layer prevents partial graphitization of the surface and leads to a well-ordered uniform surface. RHEED observation showed a sharp (2×2) pattern with strong Kikuchi lines. It is known that the SiC(0001̄) surface takes surface reconstructions of (3×3), C-rich (2×2), and Si-rich (2×2), depending on

sample preparation.¹⁴ We unveiled this surface structure consisting of Si adatoms and a Si adlayer overlying the bulk-truncated C-Si bilayer. Ni was deposited onto the (2×2) surface by MBE at a deposition rate of 1.08×10^{15} atoms/cm²/min at RT. The deposition rate was calibrated in advance by Rutherford backscattering using 2 MeV He⁺ ions.

The experiment was performed at Beamline 8 named SORIS at Ritsumeikan SR Center (Kusatsu, Japan), which combined MEIS/LEIS with SR-PES. The samples were heated by infrared radiation and the temperature was monitored with a Pt-Rh thermocouple set about 1 mm above the sample. A well-collimated He⁺ beam with energy ranging from several keV up to 130 keV was incident on a sample, and backscattered He⁺ ions were detected by a toroidal electrostatic analyzer (ESA) with an excellent energy resolution ($\Delta E/E$) of 9.0×10^{-4} . The present MEIS and LEIS analyses determined elemental depth profiles and atomic configurations near the surface region. Here it must be noted that the toroidal ESA detected only He⁺ ions. In order to determine the absolute amount of atoms of interest, we need the He⁺ fractions as a function of ion velocity. For He ions scattered from low Z atoms ($Z < \sim 20$) located near a top surface, the He⁺ fraction does not reach an equilibrium.¹⁵ So, we measured in advance the surface peaks for amorphous Si and graphite targets and obtained the nonequilibrium He⁺ fractions, which enhanced by 120 and 200%, respectively, compared with the equilibrium He⁺ fractions. The detail of the nonequilibrium charge fractions generating a surface peak for amorphous targets is described in the literature.¹⁵

Quite complementally, SR-PES analysis provides the information on electronic states of chemical bonds and valence band structures. The SR light was monochromated in the energy range from 10 to 500 eV and was incident on the sample with a beam size of 1×2 mm². Emitted photoelectrons were analyzed by a hemispherical ESA with an energy resolution of about 10 meV at a typical pass energy of 2.95 eV. The total energy resolution was estimated to be about 100 meV including the contributions from a Doppler broadening and energy spreads of incident photons. The analyzer fixed at an angle of 55° with respect to the incident beam axis detected emitted photoelectrons at acceptant angles of $\pm 2^\circ$. The emission angle was varied by rotating the sample, and normal and oblique incidence allowed s - and p -polarized photons, respectively.

III. RESULTS AND DISCUSSION

As reported previously,¹² the clean (2×2) surface consists of Si adatoms (0.25 ML) overlying a Si-adlayer (0.75ML), which is located on the first C-Si bilayer. The (2×2) spots were gradually weakened with increasing Ni coverage and almost disappeared at deposition of 0.3 ML. With Ni coverage from 0.3 to 1.3 ML, the RHEED spots are similar to a (1×3) pattern but not exactly for the samples as-grown and post-annealed at temperatures (T) up to 600°C . We tentatively call this reconstructed surface a pseudo- (1×3) structure ($[(1 \times 3)_p]$). Annealing at T from 700 to 800°C sometimes led to a (3×3) structure but not

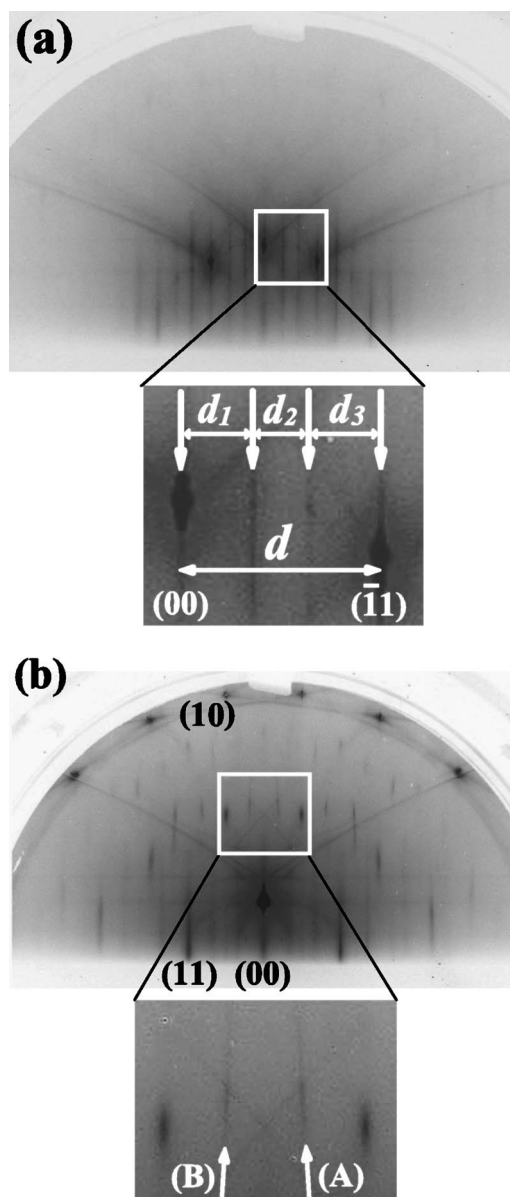


FIG. 1. RHEED patterns observed at $[11\bar{2}0]$ -azimuth (a) and $[1\bar{1}00]$ -azimuth (b) for Ni(1 ML)/SiC(000 $\bar{1}$) post-annealed at 600°C for 2 min.

always. This suggests that the (3×3) phase is not very stable energetically. Post annealing at T higher than 800°C produced a $(2\sqrt{3} \times 2\sqrt{3})$ superstructure. A SiC(000 $\bar{1}$)- (1×1) pattern was observed for the as-deposited samples with Ni coverage more than 1.3 ML and disappeared for the coverage from 3 to 5 ML. In this paper, we focus our attention on the atomic and electronic structures of the pseudo- (1×3) and $(2\sqrt{3} \times 2\sqrt{3})$ reconstructed surfaces.

A. Atomic and electronic structures of the pseudo- (1×3) surface

Figure 1 shows the RHEED patterns observed at $[11\bar{2}0]$ -azimuth (a) and $[1\bar{1}00]$ -azimuth (b) for Ni(1 ML)/

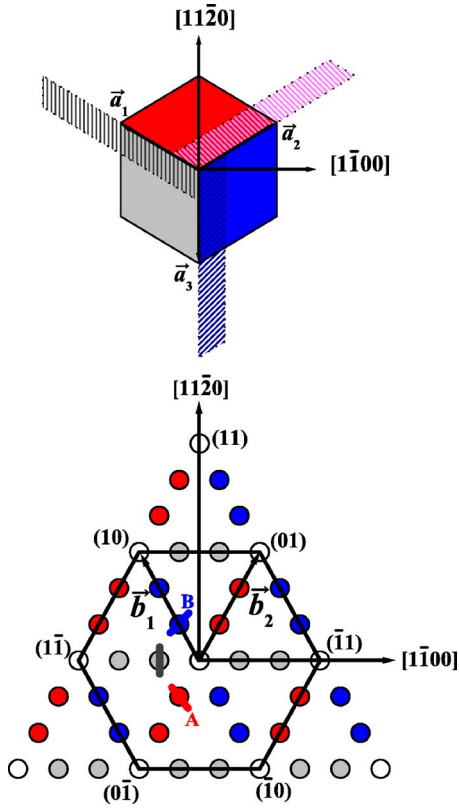


FIG. 2. (Color online) Top view of direct lattice of SiC(000 $\bar{1}$) (top) and reciprocal lattice points (bottom) obtained from RHEED observation. Red, blue, and gray domains correspond to fractional order diffraction spots with same colors.

SiC(000 $\bar{1}$) post-annealed at 600 °C for 2 min. The indices of (00), (11), and (10) represent the reciprocal lattice points of the (1 \times 1) structure. The RHEED image observed at the [11 $\bar{2}$ 0]-azimuth has additional two streaky spots between the (00) and ($\bar{1}$ 1) spots similar to a (1 \times 3) periodicity. However, as indicated in the magnified image, the interval (d_1) between the (00) and 1/3 fractional-order spots is equal to that (d_3) between the ($\bar{1}$ 1) and 2/3 fractional-order spots but not

equal to that (d_2) between the 1/3, and 2/3 fractional-order spots. So, this pattern does not correspond to any incommensurate structures. Now, we define the ratio of $d_1(=d_3)$ to $d(=d_1+d_2+d_3)$ as p , which is a little bit larger than 1/3. The corresponding fractional-order spots were also observed at the [1 $\bar{1}$ 00] azimuth, as shown in Fig. 1(b). Such a situation is well understood, if we consider equivalent three types of domains matching the SiC(000 $\bar{1}$) plane with the primitive translational vectors, (\vec{a}_1, \vec{a}_2), (\vec{a}_2, \vec{a}_3), and (\vec{a}_3, \vec{a}_1), as shown in Fig. 2 (top), because the (000 $\bar{1}$)-2 \times 2 surface has three-fold rotational symmetry (C_{3v}). So, we classify the fractional reciprocal lattice points into three categories corresponding to the above three types of domains, as indicated by red, blue and gray circles in Fig. 2 (bottom). In the case of the red reciprocal lattice points, the reciprocal lattice vectors are expressed by

$$\vec{G} = m\vec{b}_1 + n\vec{b}_2 \pm p\vec{b}_2, \quad (1)$$

where m and n are integers. The reciprocal lattice vectors given by $m\vec{b}_1 + n\vec{b}_2$ indicate the (1 \times 1) spots. Now, we perform the Fourier transform from the reciprocal lattice vectors into the direct lattice ones, for example, for the fractional order diffraction spots depicted by the red circles in Fig. 2 (bottom). The scattering density $\rho(\vec{r})$ is expressed by

$$\rho(\vec{r}) = \sum_G \rho_G \exp(-i\vec{G} \cdot \vec{r}), \quad (2)$$

where the Fourier coefficient ρ_G is assumed to be constant for simplicity. Figure 3 shows the calculated periodicity in the direct lattice along the directions of \vec{a}_1 (top) and \vec{a}_2 vectors for p values of 1/3, 0.34, 0.35, 0.36, 0.37, and 0.38 from the top to the bottom. As expected, the (1 \times) periodicity emerges along the direction of \vec{a}_1 for any p values. In the direction along \vec{a}_2 , however, the onefold, twofold, and threefold structures appear except for $p=1/3$. The scattering density $\rho(\vec{r})$ has a periodic structure even for a p value larger than 1/3. Apparently, with increasing the p -value, the period of $\rho(\vec{r})$ and the frequency of the threefold periodicity decreases and conversely the frequency of the onefold and two-

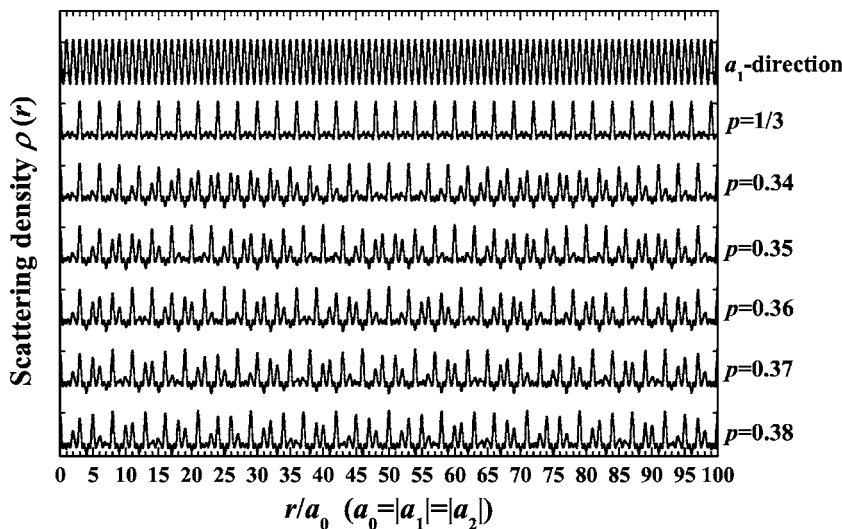


FIG. 3. Calculated scattering density $\rho(r)$ along \vec{a}_1 and \vec{a}_2 vectors for p values of 1/3, 0.34, 0.35, 0.36, 0.37, and 0.38 is indicated from the top to the bottom. The top and second profiles, respectively, represent onefold periodicity along \vec{a}_1 and exact threefold periodicity along \vec{a}_2 for $p=1/3$.

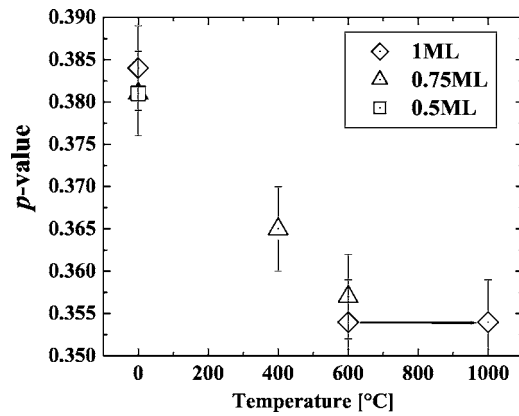


FIG. 4. p values dependent on Ni coverage and annealing temperature. Open square, triangles, and diamonds denote Ni deposition of 0.5, 0.75, and 1.0 ML, respectively.

fold periodicity increases. Of course, p value of just $1/3$ corresponds to the ordinary (1×3) structure. Here, we must note that the arrangement of the $(\times 1)$, $(\times 2)$, and $(\times 3)$ supercells along \vec{a}_2 is basically random, although it reflects the periodicity of $\rho(\vec{r})$, because $\rho(\vec{r})$ represents the probability of occupying the lattice site along \vec{a}_1 and \vec{a}_2 . Such a microscopic phase mixture in each domain was reported previously for Ca(1–3 ML)/Si(111) post annealed at 700–800 °C.¹⁶ The p value is dependent on annealing temperature but not on Ni coverage, as shown in Fig. 4. The p value decreases with increasing annealing temperature and is saturated at 600 °C, and stepwise annealing from 600 °C up to 1000 °C does not change the $[1 \times 3]_p$ structure and the p value. On the other hand, the $[1 \times 3]_p$ surfaces formed at 400 °C or less changed into the $2\sqrt{3} \times 2\sqrt{3}$ reconstruction.

Another interesting phenomenon observed in the RHEED patterns is the fact that some streaks of the fractional order diffraction spots are not parallel to the reciprocal rods and slightly inclined toward the central line including the (00) rod with an axial symmetry, as seen in Fig. 1(b). Let us pay an attention to the inclined streaks of A and B, for example, indicated in the magnified image. These two streaks of A and B come from the reciprocal rods of A (red) and B (blue) in Fig. 2 (bottom). The reciprocal rod (A) gives such an inclined streak toward the central line, if the length of the domain along \vec{a}_2 is much larger than that along \vec{a}_1 , as illustrated by dashed red lines (slender rectangle shape) in Fig. 2 (top). For such anisotropic domains with the primitive translation vectors (\vec{a}_1, \vec{a}_2) , the cross section of the reciprocal rod intersected by the Ewald sphere has a short axis along \vec{b}_2 and a long axis along \vec{b}_1 and thus the inclined streaks emerge. The incline of the streak B coming from the blue domain is also explained in the same manner. Thus it is seen that there are actually three types of domains taking slender rectangle shapes with long edges along the $[\bar{1}\bar{2}\bar{1}0]$ ($[\bar{1}\bar{2}10]$), $[\bar{1}\bar{1}20]$ ($[\bar{1}1\bar{2}0]$), and $[2\bar{1}\bar{1}0]$ ($[\bar{2}110]$) directions [see the shapes drawn by dashed lines of red, blue, and gray in Fig. 2 (top)]. The domain length along \vec{a}_1 ($1 \times$) should be considerably smaller than the coherent zone size (several hundreds Å) in the present RHEED observation.

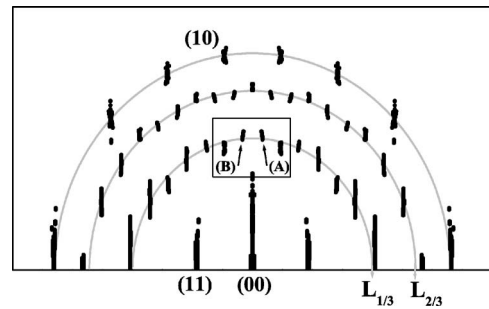


FIG. 5. Simulated RHEED pattern at the $[1\bar{1}00]$ azimuth obtained by superimposing the plane waves scattered from Ni (Si) atoms making the $[1 \times 3]_p$ structure obtained for a p value of 0.35. The domain lengths along \vec{a}_1 and \vec{a}_2 are assumed to be 61.6 and 369.6 Å, respectively for the red domain. Quite the same condition is adopted for blue and gray domains.

Such a situation is confirmed by superimposing the plane waves scattered from Ni (Si) adatoms making anisotropic three types of domains with slender shapes. The lattice site occupations were determined by generating random numbers, reflecting the scattering densities $\rho(\vec{r})$. Figure 5 is the simulated RHEED pattern at the $[1\bar{1}00]$ -azimuth assuming the $[1 \times 3]_p$ structure with a p value of 0.35. The lengths along \vec{a}_1 and \vec{a}_2 were assumed to be 61.6 and 369.6 Å, respectively, for the red domain. The conditions for the other two types of domains are quite the same as that for the red domain. The simulated pattern coincides well with the observed one, if the domain length along \vec{a}_2 (\vec{a}_3) is assumed to be more than three times larger than that along \vec{a}_1 (\vec{a}_2) for the red (blue) domain.

Figure 6 shows the MEIS spectra observed for 120 keV He^+ ions incident on the Ni(1 ML)/SiC(000 $\bar{1}$) post-annealed

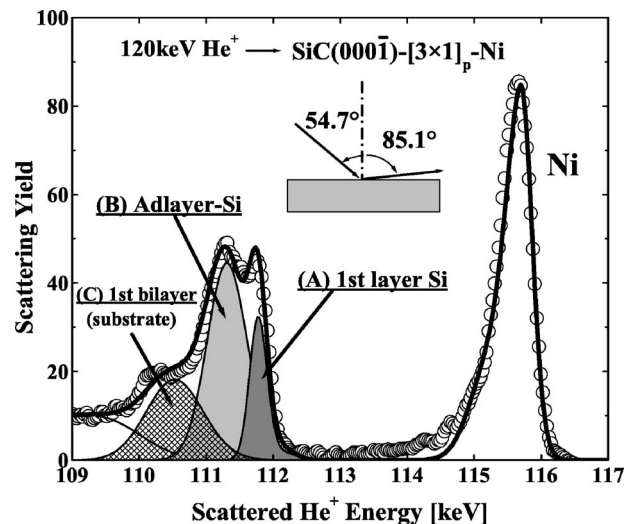


FIG. 6. MEIS spectrum observed for 120 keV He^+ ions incident on Ni(1 ML)/SiC(000 $\bar{1}$) post-annealed at 600 °C for 2 min. Thick and thin solid curves are total and decomposed spectra, respectively best fitted to the observed spectrum (open circles). Incident and detection angles were set to 54.7° ($[044\bar{1}]$ axis) and 85.1° with respect to surface normal, respectively.

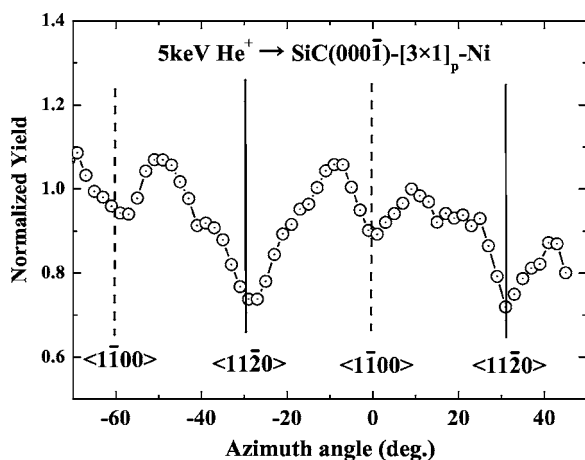


FIG. 7. Azimuth-scan spectrum observed using 5 keV He^+ ions for the scattering component from Ni. Incident and emergent angles were 40° and 85° with respect to surface normal, respectively. Azimuth angles of (0, 60° and 120°) and (30° and 90°) correspond to the $[1\bar{1}00]$ and $[1\bar{1}\bar{2}0]$ directions, respectively.

at 600°C for 2 min. The incident and detection angles were set to 54.7° (corresponding to the $[04\bar{4}\bar{1}]$ axis) and 85.1° with respect to surface normal, respectively. The amount of Ni on top of the surface is estimated to be 0.40 ± 0.05 ML for the 600°C -annealed sample, indicating that 0.6 ML Ni atoms were lost from the top surface. The surface peak from Si has mainly three components of (A), (B), and (C). First, we consider the origin of the component denoted by (C). The energy shift of (C) scaled from the energy position ($E_{\text{Si}}^{\text{surf}}$) for scattering from the surface Si is almost equal to that of the carbon surface peak scaled from $E_{\text{C}}^{\text{surf}}$. Thus, the component (C) originates from Si atoms in the first C-Si bilayer. Considerable reduction of the scattering yield from that expected for 1 ML Si is caused by the shadowing of some overlayers. Therefore, the components (A) and (B) come from Si adatoms (0.40 ± 0.05 ML) and Si adlayer (0.80 ± 0.05 ML), respectively. The difference between the heights of the Ni and Si adatoms is not resolved clearly as an energy shift by the present MEIS analysis. However, the width of the Ni surface peak suggests that the topmost layer consists of the same number (~ 0.4 ML) of Si and Ni adatoms. As mentioned earlier, the $[1 \times 3]_p$ pattern was also observed for Ni(0.3–1.3 ML)/SiC(000 $\bar{1}$) as-deposited and post-annealed at 400°C . In these cases, MEIS analysis shows no loss of Ni from the surface. So, the $[1 \times 3]_p$ structure is formed in an early stage and relatively stable against further Ni deposition up to coverage of 1.3 ML. Post-annealing at higher temperatures makes excess Ni atoms diffuse inside or escape from the surface.

In order to determine the atomic configuration, we measured the scattering yields from Ni as a function of azimuth angle using 5 keV He^+ ions. Low-energy ion scattering is very sensitive to atomic configurations of topmost layers because of making large shadow cones. Figure 7 shows the azimuth scan spectrum measured with 5 keV He^+ ions for the $[1 \times 3]_p$ surface formed by annealing at 600°C . The incident and emergent angles were set to 40° and 85°

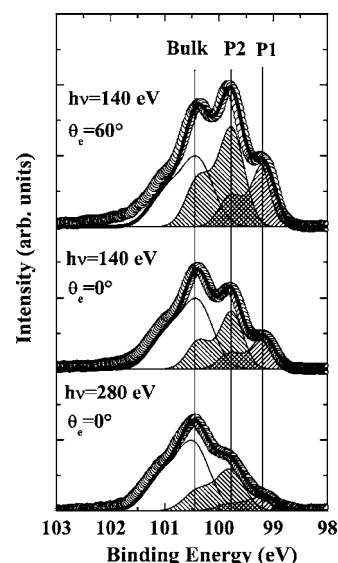


FIG. 8. Si $2p_{1/2,3/2}$ core level spectra taken at photon energy of 140 and 280 eV for Ni(1 ML)/SiC(000 $\bar{1}$) post-annealed at 600°C for 2 min. Emission angles scaled from surface normal were 60° (top), 0° (middle), and 0° (bottom). Spectra were decomposed into three components, bulk and two surface-related ones (P1 and P2). The binding energy is scaled from the Fermi level.

with respect to surface normal, respectively. The scattering yields were considerably reduced for incidence along the $[1\bar{1}\bar{2}0]$ azimuth with sixfold symmetry. This indicates an ordered structure of Ni along this axis making one-dimensional atomic chains with the $(1 \times)$ periodicity. Of course, the $(\times 1)$, $(\times 2)$, and $(\times 3)$ periodicity appear along the $[\bar{2}110]$ axis. Three different three domains [see Fig. 2 (top)] having the stripe structure contribute to the rotational symmetry as shown in Fig. 7. The significant reduction of the scattering yields at the $[1\bar{1}00]$ azimuth is probably due to some blocking effect by either the Si adatoms or the Ni adatoms with the $(\times 1)$ and $(\times 2)$ structures.

We observed the Si $2p$ core level spectra for the $[1 \times 3]_p$ surface and found two surface related components (P1 and P2) other than the bulk component (see Fig. 8). The binding energies scaled from the Fermi level (E_F) are 99.2, 99.8, and 100.6 eV, respectively, for P1, P2, and bulk components. Considering the escape depth, the intensity ratio of P1 to P2 is estimated to be ~ 0.5 . This ratio coincides with that of the number of adatom-Si (0.4 ML) to adlayer Si (1 ML) estimated from the MEIS analysis. Therefore, P1 and P2 originate from the Si adatoms and Si adlayer, respectively. The C $1s$ spectra is observed have a single component, suggesting that the C atoms in the top C-Si bilayer make a stable bond with the adlayer Si atoms. We also measured the valence band spectra for the $[1 \times 3]_p$ surface at normal emission by varying incident photon energy, as indicated in Fig. 9. It is found that the $[1 \times 3]_p$ surface has a metallic character and the peaks about 2 eV below the Fermi level originate from the Ni $3d$ band because of its localized (nondispersive) nature and the intensity dependent on photon energy [photoionization cross section for d electrons takes a

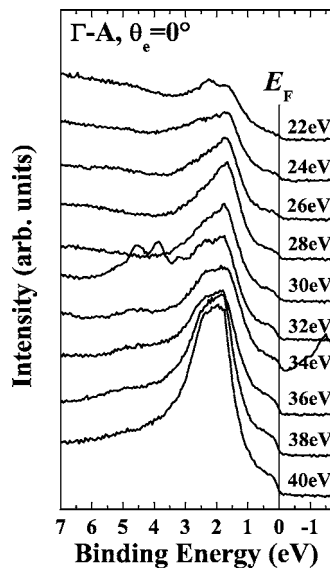


FIG. 9. Valence band spectra taken at photon energies from 22 to 40 eV under normal emission condition. The binding energy is scaled from the Fermi level.

maximum value at photon energy ~ 40 eV (Ref. 17)].

B. Atomic and electronic structures of the $2\sqrt{3}\times 2\sqrt{3}$ surface

As mentioned previously, the $(2\sqrt{3}\times 2\sqrt{3})$ reconstruction appears by post annealing at temperatures higher than 800°C , which is stable up to 1000°C . Figure 10 shows the MEIS spectrum observed for 120 keV He^+ ions incident on $\text{Ni}(0.5\text{ ML})/\text{SiC}(000\bar{1})$ post-annealed at 800°C for 2 min. The incident and exit angles were set to 54.7° and 85.1° , respectively. The absolute amount of Ni on top is derived to be 0.22 ± 0.05 ML. The Si surface peak consists of three components denoted by (A), (B), and (C). The inelastic energy loss is estimated to be ~ 1 keV for He^+ ions scattered

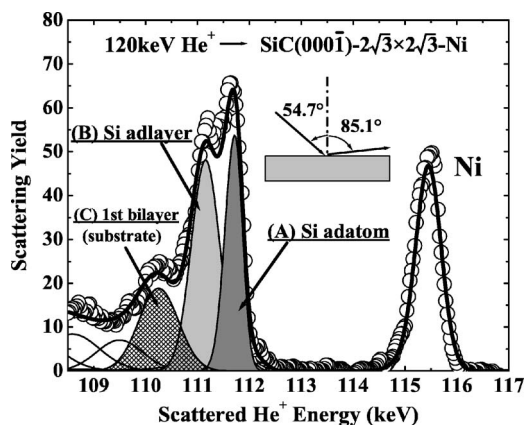


FIG. 10. MEIS spectrum observed for 120 keV He^+ ions incident on $\text{Ni}(0.5\text{ ML})/\text{SiC}(000\bar{1})$ post annealed at 800°C for 2 min. The thick and thin solid curves are total and decomposed spectra, respectively best fitted to the observed one (open circles). Incident and detection angles were set to 54.7° ($[044\bar{1}]$ -axis) and 85.1° with respect to surface normal, respectively.

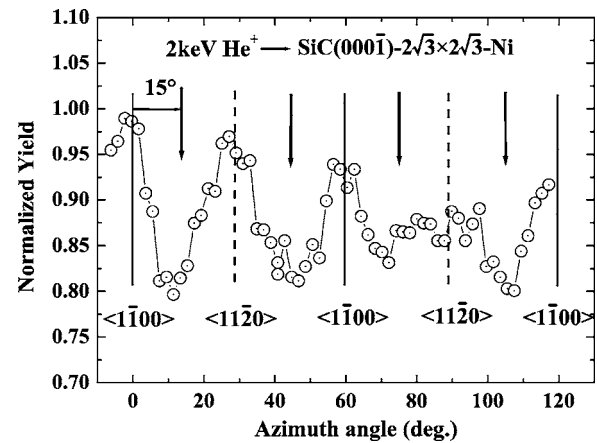


FIG. 11. Azimuth-scan profile observed for the scattering component from Ni using 2 keV He^+ ions. Azimuth angles of 0, 60, and 120° correspond to the $[1\bar{1}00]$ direction and 30 and 90° the $[11\bar{2}0]$ direction. Incident and detection angles are 0 and 70° , respectively, scaled from surface normal.

from carbon atoms in the first C-Si bilayer and thus there exist Ni and additional Si atoms overlying the first bilayer. A lower energy shift of the component (C) shows that it comes from the Si atoms in the first bilayer. The best fit of the simulated MEIS spectrum to the observed one results in the surface structure consisting of Si adatoms (0.57 ± 0.05 ML) overlying a Si adlayer (1 ML). A significant broadening of the Ni surface peak compared with that for the $[1\times 3]_p$ surface indicates that the Ni atoms (0.22 ± 0.05 ML) take a position slightly lower than the Si adatoms. Here, it must be noted that the $(2\sqrt{3}\times 2\sqrt{3})$ unit cell has 12 atoms in the $(000\bar{1})$ plane and thus the numbers of the Si and Ni adatoms in the unit cell are deduced to be 6.84 ± 0.6 and 2.64 ± 0.6 , respectively.

Figure 11 shows the azimuth-scan profile observed for the scattering component from Ni using 2 keV He^+ ions. Here, He^+ ions were incident from the normal direction and scattered to 70° from the surface normal. The azimuth-scan profile was not changed by reversing the scattering geometry. It is clearly seen that the scattering yield decreases in the scattering planes rotated by $\sim 15^\circ$ from $\{11\bar{2}0\}$ and quite equivalently from $\{1\bar{1}00\}$. This demonstrates the Si adatoms taking a significantly higher position than the Ni adatoms. The surface probably takes the C_{3v} symmetry, which results in a most stable state energetically. In addition, the C 1s spectra have a single component, suggesting a stable bonding between the Si adlayer (1 ML) and the top C-Si bilayer. Considering the C_{3v} symmetry and the results obtained above, the $(2\sqrt{3}\times 2\sqrt{3})$ surface is expected to be a structure similar to the $\text{Si}(111)-\sqrt{19}\text{Ni}$ surface,^{18,19} because the $\sqrt{19}\times\sqrt{19}$ unit cell proposed has also C_{3v} symmetry and three Ni atoms. In addition, the Si adlayer is stably connected to the underlying C-Si bilayer and thus is probably close to the Si(111) plane, although the atomic spacing is significantly different. Therefore, we propose a most probable surface structure, as indicated in Figs. 12(a) and 12(b). The *ab initio* calculations using the CASTEP code²⁰ predict a

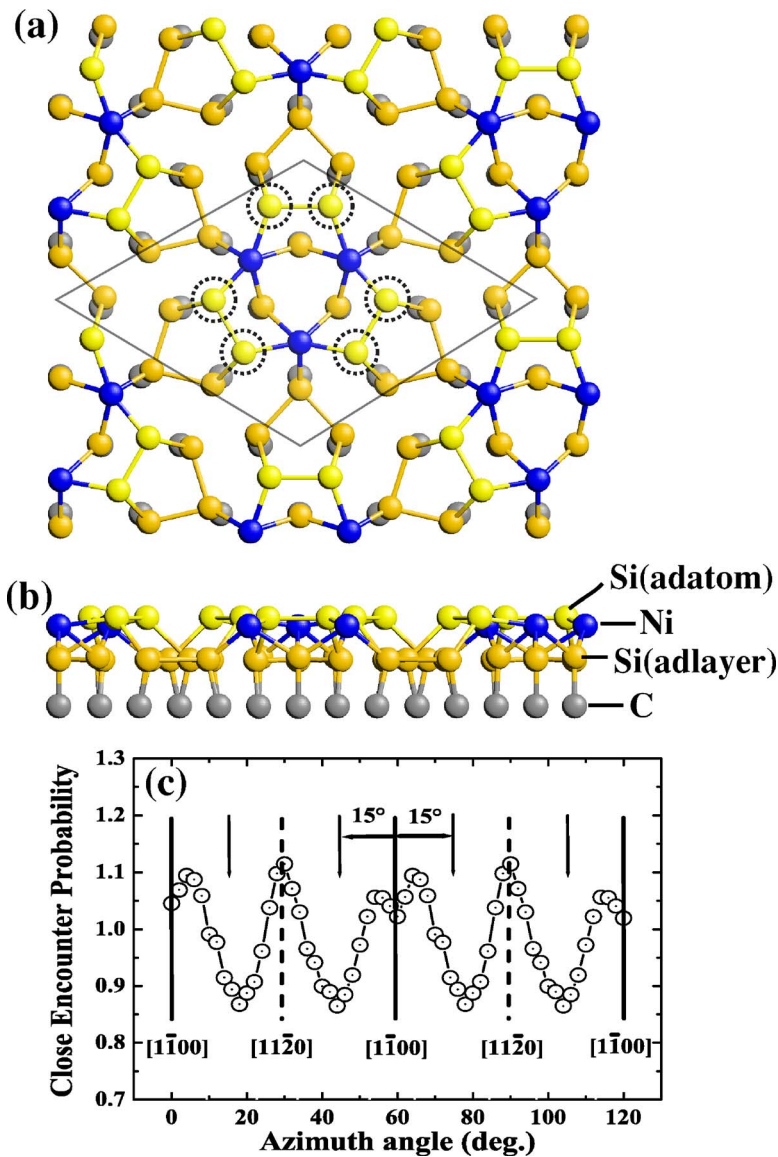


FIG. 12. (Color online) Top (a) and side (b) views of proposed surface structure for the $(2\sqrt{3} \times 2\sqrt{3})$ surface. Blue, yellow, and gray circles denote Ni, Si, and C atoms, respectively. Yellow circles surrounded by dotted circles correspond to Si adatoms. Azimuth-scan profile calculated from Monte Carlo simulations of ion trajectories for the scattering component from Ni assuming the above surface structure (bottom).

slight distortion of the Si adlayer (1 ML). The number (6) of the Si adatoms in the unit cell is different from 6.84 ± 0.06 derived from the MEIS analysis. This is probably due to uncertainty in deconvoluting the Si surface peak mainly, which comes from a spectrum asymmetry generated by inner shell excitations²¹ and from the nonequilibrium He^+ fraction for the He ions backscattered from the top surface.²² Parikh *et al.*¹⁸ reported that the $\text{Si}(111)\sqrt{19} \times \sqrt{19}$ -Ni ring is produced by quenching Ni (~ 0.5 ML)/Si(111) from above 860°C , and in the $\sqrt{19}$ unit cell there are six Si adatoms forming three pairs of dimmers and three Ni atoms taking the substitutional sites in the bottom of the substrate Si bilayer. Except for the height location of the Ni adatoms, the surface structure of $\text{SiC}(000\bar{1})-2\sqrt{3} \times 2\sqrt{3}$ Ni proposed here is quite similar to that of the $\text{Si}(111)\sqrt{19}$ -Ni ring claimed by Parikh *et al.*¹⁸, but different from the structure models of Wilson and Chiang²³ and of Ichinokawa *et al.*¹⁹ The different surface periodicity is ascribed to different bond lengths of the underlying Si layers. According to the *ab initio* calculations, the Si adlayer (1 ML) basically matches with the $\text{SiC}(000\bar{1}) 1 \times 1$

face except for small distortion. Figure 12(c) shows the azimuth scan profile best fitted to the one observed for the scattering component from Ni by Monte Carlo simulations of ion trajectories assuming the above surface structure. As a result, it is found that the Si adatoms take a higher position by 0.9 \AA than the Ni adatoms and the Si-dimer bond length is 2.4 \AA , which is compatible with that of Si bulk crystal (2.35 \AA) and with the dimer bond length of $\text{Si}(001)-2 \times 1$ (2.28 \AA).

Figure 13 shows the valence band spectra for the $\text{SiC}(000\bar{1})-(2\sqrt{3} \times 2\sqrt{3})$ -Ni surface taken at photon energy of 40 eV . The spectra were measured along the $\bar{\Gamma}-\bar{M}$ direction of the $\text{SiC}(000\bar{1})-(1 \times 1)$ corresponding to the $\bar{\Gamma}-\bar{K}-\bar{M}$ direction of the $2\sqrt{3} \times 2\sqrt{3}$ surface. The surface electronic state shows a nonmetallic character, in contrast to the $[1 \times 3]_p$ phase. The valence band maximum is estimated to be about 1.8 eV below E_F of $\text{SiC}(000\bar{1})$ and thus the states of A ($\sim 1.2 \text{ eV}$) and B ($\sim 1.7 \text{ eV}$) are located in the band gap. Figure 14 shows the valence band spectra as a function of incident photon energy observed at surface normal direction.

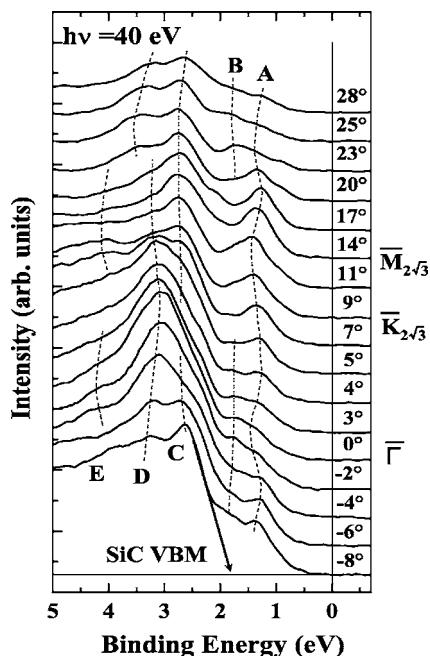


FIG. 13. Valence band spectra observed for the $(2\sqrt{3}\times 2\sqrt{3})$ surface at photon energy of 40 eV. Varying the emission angle allows determination of the surface band structure along the $\bar{\Gamma}-\bar{M}$ direction of SiC(0001)-(1 \times 1). The binding energy is scaled from the Fermi level.

The peaks denoted by A–E are not dispersed significantly, indicating two-dimensional electronic states. As mentioned previously, photoionization cross sections for d -orbital electrons generally take a maximum value around 40 eV.¹⁷ Quite

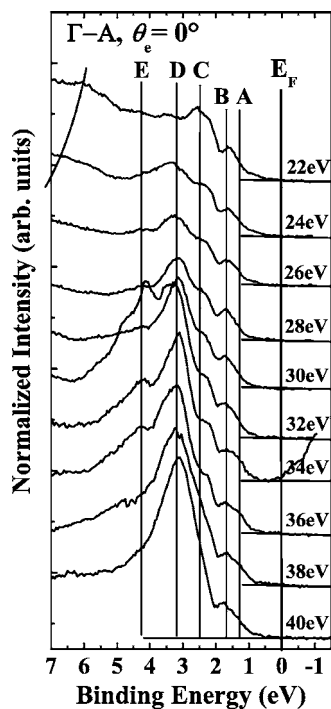


FIG. 14. Valence band spectra observed for the $(2\sqrt{3}\times 2\sqrt{3})$ surface under normal emission condition varying incident photon energy.

differently, those for s and p orbitals are drastically increased with decrease in incident photon energy. So, the peaks D and E originate from the Ni $3d$ orbital. On the other hand, the peak intensities of A and B are almost constant in the observed energy range (no dispersion) and were significantly reduced by O_2 exposure of 10 L.

We also measured valence band spectra at incident angles of 70° , 40° , and 0° with respect to surface normal. The SR light was linearly polarized in the horizontal plane and the sample was rotated around a vertical axis perpendicular to surface normal. So, normal and oblique incidence provides s - and p -polarized photons, respectively. Thus normal incidence prevents the photoemission from the electron orbitals extending in the normal direction (z axis) because of the dipole selection rule. The intensity of the intergap state (A) is strongly dependent on photon polarization and reduces remarkably at normal incidence. Therefore, the surface state (A) with a strong p_z character should originate from dangling bonds of the topmost Si adatoms. This result supports our structure model, because each of the six Si adatoms in the unit cell has one dangling bond (see Fig. 12). Such a non-metallic and semiconductorlike character is explained well by assuming the above structure model. In fact, overlapping of the Ni $3d$ electron clouds in different unit cells is negligibly small because of a large interatomic distance for the Ni adatoms more than 10.7 Å.

IV. CONCLUSION

The atomic and electronic structures of the 6H-SiC(0001)- 2×2 surface deposited with an ultrathin Ni(0.3–1.3 ML) layer before and after annealing were analyzed by high-resolution MEIS/LEIS, SR-PES, and RHEED. The RHEED observation for the Ni/SiC(0001) as-deposited and post-annealed ($T\leq 600^\circ\text{C}$) showed the pseudo-(1 \times 3) ($[1\times 3]_p$) patterns. Detailed quantitative analysis reveals basically random arrangement of the (1 \times 1), (1 \times 2), and (1 \times 3) supercells in each domain. The surface consists of three equivalent types of domains taking slender rectangle shapes with long edges $[p-(\times 3)]$ parallel to the $[\bar{1}2\bar{1}0]$, $[\bar{1}\bar{1}20]$, and $[2\bar{1}10]$ directions and correspondingly with short edges (1 \times) along the $[2\bar{1}\bar{1}0]$, $[\bar{1}2\bar{1}0]$, and $[\bar{1}\bar{1}20]$, respectively. It is also found that Ni adatoms on top of the surface are aligned along the $[11\bar{2}0]$ direction to form one-dimensional (1 \times) chains. The valence band spectra show that the $[1\times 3]_p$ surface has a metallic character. Post annealing at $T > 800^\circ\text{C}$ leads to the $(2\sqrt{3}\times 2\sqrt{3})$ structure. The MEIS analysis reveals the fact that Si (0.57 ML) and Ni (0.22 ML) adatoms are located on the Si adlayer (1 ML) terminating the first C-Si bilayer. The azimuth-scan analysis using 2 keV He^+ ions unveils the surface structure quite resembling that of the Ni/Si(111)- $\sqrt{19}$ rings proposed by Parikh, Lee, and Bennett.¹⁸ Stable but relatively flexible bonding between the Si adlayer (1 ML) and the underlying C-Si bilayer makes it possible. Best-fitting the MC-simulated azimuth scan profile to the observed one shows that the Si adatoms take a higher position by 0.9 Å than the Ni adatoms and the Si-dimer bond

length is 2.4 Å, which is compatible with that of Si bulk crystal. The valence band spectra show that the surface has a nonmetallic property, in contrast to the $[1 \times 3]_p$ surface. Such a nonmetallic and semiconductorlike character is responsible, for the large interatomic distance more than 10.7 Å for the Ni adatoms in the neighboring $2\sqrt{3} \times 2\sqrt{3}$ unit cells.

In both cases ($[1 \times 3]_p$ and $2\sqrt{3} \times 2\sqrt{3}$), the surfaces take adatoms/adlayer structures. This is attributed to the original Si-rich SiC(000 $\bar{1}$)- 2×2 surface taking the adatoms/adlayer structure. In contrast, Ni(1 ML)/SiC(0001)- $\sqrt{3} \times \sqrt{3}$ surfaces before and after annealing take quite different structures.^{9–11} The SiC(0001)- $\sqrt{3} \times \sqrt{3}$ surface has 1/3 ML Si on the top [Si-C]-bilayer. Such an Si-adatoms-[Si-C](bilayer) structure

looks similar to the Si-adatoms-(Si-adlayer)-[C-Si] (bilayer) surface. The different surface structures are probably ascribed to the stable but relatively flexible bonding between the Si adlayer and the [C-Si] bilayer compared with the strong bonding of the [Si-C] bilayer.

ACKNOWLEDGMENTS

The authors would like to thank Professor H. Namba and Dr. K. Ogawa for maintaining the SR-PES system of BL-8 at Ritsumeikan SR Center. Special thanks are also due to Dr. T. Okazawa and Mr. R. Fukuyama for their help in the MEIS experiment.

*E-mail address: yht23389@se.ritsume.ac.jp

¹*SiC Materials and Devices*, Vol. 52 of *Semiconductors and Semimetals*, edited by Y. S. Park (Academic Press, San Diego, 1998).

²L. M. Porter and R. F. Davis, *Mater. Sci. Eng.*, B **34**, 83 (1995).

³J. Crofton, P. G. McMullin, J. R. Williams, and M. J. Bozack, *J. Appl. Phys.* **77**, 1317 (1995).

⁴T. Teraji and S. Hara, *Phys. Rev. B* **70**, 035312 (2004).

⁵W. Platow, D. K. Wood, K. M. Tracy, J. E. Burnette, R. J. Nemanich, and D. E. Sayers, *Phys. Rev. B* **63**, 115312 (2001).

⁶A. Ohi, J. Labis, Y. Morikawa, T. Fujiki, M. Hirai, M. Kusaka, and M. Iwami, *Appl. Surf. Sci.* **190**, 366 (2002).

⁷S. Y. Han, J.-Y. Shin, B.-T. Lee, and J.-L. Lee, *J. Vac. Sci. Technol. B* **20**, 1496 (2002).

⁸K. Fukuda, S. Suzuki, T. Tanaka, and K. Arai, *Appl. Phys. Lett.* **76**, 1585 (2000).

⁹Y. Hoshino, O. Kitamura, T. Nakada, and Y. Kido, *Surf. Sci.* **539**, 13 (2003).

¹⁰Y. Hoshino, S. Matsumoto, and Y. Kido, *Phys. Rev. B* **69**, 155303 (2004).

¹¹Y. Hoshino, S. Matsumoto, T. Nakada, and Y. Kido, *Surf. Sci.* **556**, 78 (2004).

¹²Y. Hoshino, R. Fukuyama, Y. Matsubara, T. Nishimura, S.

Tanaka, M. Kohyama, and Y. Kido, *Phys. Rev. B* **71**, 195331 (2005).

¹³W. Kern and D. A. Poutinen, *RCA Rev.* **31**, 187 (1970).

¹⁴J. Bernhardt, A. Seubert, M. Nerding, U. Starke, and K. Heinz, *Mater. Sci. Forum* **338–342**, 345 (2000).

¹⁵Y. Kido, T. Nishimura, and F. Fukumura, *Phys. Rev. Lett.* **82**, 3352 (1999).

¹⁶F. Shimokoshi, I. Matsuda, S. Hasegawa, and S. Ino, *e-J. Surf. Sci. Nanotechnol.* **2**, 178 (2004).

¹⁷J. J. Yeh and I. Lindau, *At. Data Nucl. Data Tables* **32**, 1 (1985).

¹⁸S. A. Parikh, M. Y. Lee, and P. A. Bennett, *Surf. Sci.* **356**, 53 (1996).

¹⁹T. Ichinokawa, T. Tani, and A. Sayama, *Surf. Sci.* **219**, 395 (1989).

²⁰M. C. Payne, M. P. Teter, D. A. Allan, T. A. Arias, and J. D. Joannopoulos, *Rev. Mod. Phys.* **64**, 1045 (1992).

²¹Y. Kido, S. Semba, and Y. Hoshino, *Nucl. Instrum. Methods Phys. Res. B* **219–220**, 599 (2004).

²²Y. Hoshino, S. Semba, T. Okazawa, and Y. Kido, *Surf. Sci.* **515**, 305 (2002).

²³R. J. Wilson and S. Chiang, *Phys. Rev. Lett.* **58**, 2575 (1987).